Soft Matter

Correlation between morphology and anisotropic transport properties of diblock copolymers melts

Journal:	*Soft Matter*
Manuscript ID	SM-ART-10-2018-002095.R1
Article Type:	Paper
Date Submitted by the Author:	21-Nov-2018
Complete List of Authors:	Alshammasi, Mohammed; Cornell University, Robert Frederick Smith School of Chemical and Biomolecular Engineering Escobedo, Fernando; Cornell University, School of Chemical and Biomolecular Engineering

Correlation between morphology and anisotropic transport properties of diblock copolymers melts

Mohammed Suliman Alshammasi and Fernando A. Escobedo*

Robert Frederick Smith School of Chemical and Biomolecular Engineering, Cornell University, Ithaca, NY 14853, USA

Abstract

Molecular simulations of coarse-grained diblock copolymers (DBP) were conducted to study the effect of segregation strength and morphology on transport properties. It was found that in the strong segregation limit (i.e., high χN, where χ is the Flory-Huggins parameter and N is the degree of polymerization), the presence of the DBP interfaces imposes topological constraints similar to those of entanglements as manifested in the rheological signature of the polymer (i.e., a plateau modulus). Furthermore, compared to the behavior of isotropic melts, the crossover from Rouse to reptation scaling of the self-diffusion coefficient (D) parallel to the DBP interface takes place at a smaller N, an effect that depends on temperature and is more pronounced in the Lamellae morphology than in the Hexagonal Cylinder morphology. Additionally, it is shown that for an entangled melt (i.e., $N \gg N_e$ where N_e is the entanglement length) block retraction is instrumental for chains to diffuse parallel to the interface of lamellar layers. Lastly, it is found that the anisotropic viscosity of different morphologies is mostly affected by the orientation of the chains relative to the shear flow direction, exhibiting reduced values when chains align in the neutral or flow directions.

Introduction

In microphase separated phases of diblock copolymers (DBP), naturally conflicting properties are able to exist in nanoscale proximity, which makes these materials attractive for applications ranging from lithography to artificial organ technology, drug delivery, and energy storage.[1,2] For example, the mechanical stability of solid polymer electrolytes used in battery applications is essential for sustainable and safe operations.[3] DBPs have been thoroughly studied as a potential materials' platform to improve electrolyte stability and safety.[4,5,6,7] While the conductive block is typically flexible and contains polar sites that can solvate salts, the other non-polar block can be made rigid or glassy to impart the system with the mechanical stability needed to suppress dendrite formation. In drug delivery applications, DBPs with hydrophilic and hydrophobic blocks can be utilized in order to transport hydrophobic drugs in the bloodstream at concentrations

above their intrinsic water solubility limit. The hydrophilic block forms a protective shell against bio-degradation of the bioactive molecules enhancing the drug integrity and performance. Additionally, the reversible nature of the temperature-driven DBPs ordering (i.e., from order to disorder and vice versa) allows for thermally controlled release of the bioactive molecules[2]. Hence, characterizing viscoelastic and dynamic properties of DBPs (which correlate with mechanical stability and ordering kinetics) is of critical importance from both fundamental and application perspectives. Furthermore, studying model DBP systems of linear chains could provide insights relevant to other more complex DBP resembling systems, such as polymer-grafted nanoparticles, polymer brushes,[8] and protein lipid bilayers.

In the past few decades, theoreticians and experimentalists have devoted much attention to understanding the dynamic and viscoelastic properties of homopolymers melts, and their departure from those of small organic liquids. One important parameter that largely influences the viscoelastic behavior of melts of linear homopolymer is the degree of polymerization (N). The self-diffusion coefficient (D) follows a $N^{-\xi}$ scaling, where ξ is 1 in the Rouse regime (consistent with the Einstein Diffusion model), and 2 in the reptation regime (consistent with de Gennes' tube model), while the zero-shear viscosity (η_0) follows a N^{ξ} scaling, where ξ is 1 in the Rouse regime, and 3 in the reptation regime.[9] In the Rouse regime (i.e., below the entanglement chain length, N_e), the polymer chains can slide past one-another. Such diffusion mechanism does not take place when $N > 2N_e$ due to the constraints imposed by the melt that confine a particular chain to a tube whose diameter (d_T) can be correlated with the end-to-end distance of a chain with N_e segments (i.e. $d_T \approx aN_e^{1/2}$, where a is the Kuhn length).[10] Entanglements only allow for diffusion along the contour of the tube, whose length is l, within which the chain-end 'reptates' from one tube to the next following the path taken by other segments of the chain. Within a tube, the polymer segments locally diffuse following the Rouse model; however, for the whole chain to diffuse it needs to travel a distance l as opposed to its end-to-end distance in "unentangled" polymer melt, thereby increasing the relaxation time of the chain and giving rise to the reptation scaling regime. The theoretical scaling predictions in the Rouse and reptation regimes for both D and η_0 were found to explain experimental and computational results for homopolymer melts with only a slight difference in the ξ exponent observed in the reptation

regime.[11,12,13] The D scaling with N is more sensitive to entanglements than that of η_0 since the Rouse contribution to η_0 is strong and it is only for $N \gg N_e$ that the exponential component, arising from entanglement, becomes dominant.[13]

While the dependence of dynamic and viscoelastic properties on a wide spectrum of parameters (i.e., temperature, concentration, and chain length), and polymer designs (i.e., branching) is well understood for homopolymer melt systems,[14,15,16,17] it is less so for DBP systems. Depending on the volume fraction of the minority block (ϕ_1), and the segregation strength (χN, where χ is the Flory-Huggins parameter), linear A-B DBPs form various micro-segregated structures below the order-disorder temperature (T_{ODT}). The presence of interfaces and confining domains in such structures gives rise to additional energetic and entropic barriers that influence the transport and viscoelastic properties of DBPs.[18]

It was previously suggested that in the entangled regime, strongly segregated DBPs (i.e., for $\chi N \gg (\chi N)_{\mathrm{ODT}}$, where $(\chi N)_{\mathrm{ODT}}$ is χN at the order-disorder transition (ODT)) with Lamellae (L) morphology (i.e., $\phi_1 = 0.5$) diffuses parallel to the interface by a block retraction mechanism (where one block retracts to the interface before lateral diffusion along the interface can take place).[19,20] However, this block retraction mechanism was not observed in the simulation study of Murat et al., who argued that Lamellae-forming DBPs have reduced entanglement density compared to homopolymers due to the increased ordering in the system.[21,22] Using Kinetic Monte Carlo simulations, Pan et al. examined DBPs with L morphology and found, by comparing D for a wide range of N at a fixed low χN, that the Rouse to reptation scaling crossover chain length (N_c) for DBP is the same as that for the homopolymer.[23] Most recently, Sethuraman et al.[24] and Ramirez-Hernandez et al.[25] used topological analysis to identify entanglements in lamellae-forming DBPs. They found that N_e in DBPs (≈ 40) is slightly lower than in homopolymers (≈ 44).[25] While the dynamic properties of DBPs have been the subject of several experimental studies, it is very difficult to deconvolute the anisotropic diffusion tensor components arising from the spatial orientation of the interfaces, due to both the presence of multiple grain orientations seeded during phase microsegregation, and the different block chemistries used which potentially have different N_e.[20,26]

The stability of DBP phases under simple and oscillatory shear has been the subject of several studies.[27,28,29,30,31] Depending on the shear rate and shear orientation (Figure 1), the DBP may exhibit transitions to different orientational states and to the disordered state. The dependence of the anisotropic viscosity tensor components on morphology has only been investigated in a few computational studies.[32,33] Using shear-flow Dissipative Particle Dynamics (DPD) simulations, Zhang et al.[32] found that the viscosity of the L phase, when flow and velocity gradient are parallel to interface (L ∥), is lower than that of the Hexagonal Cylinders (HC), when flow is along the cylinder axis (HC ∥). Ryu et al.[33] used linear response theory to calculate the anisotropic zero-shear viscosity ($\eta_{0_{\alpha\beta}}$) for the L morphology from the stress auto-correlation function. However, they combined the transverse (L $\mathcal{T}$) and perpendicular (L ⊥) contributions into one component, despite these being fundamentally different due to the asymmetry of the structure.[31] Oscillatory shear experiments revealed that cubic DBPs, such as the Gyroid (G) phase, exhibit a modulus plateau (G^0_{cubic}) for $N < N_e$ at a frequency smaller than the rubbery plateau (G^0_N), reminiscent of the effect of entanglements. G^0_{cubic} of the G phase was found to span several decades in frequency at the terminal regime (approaching the zero-shear limit). Moreover, it was shown that randomly oriented L and HC phases exhibit a behavior intermediate between that of cubic phases and isotropic melts.[34]

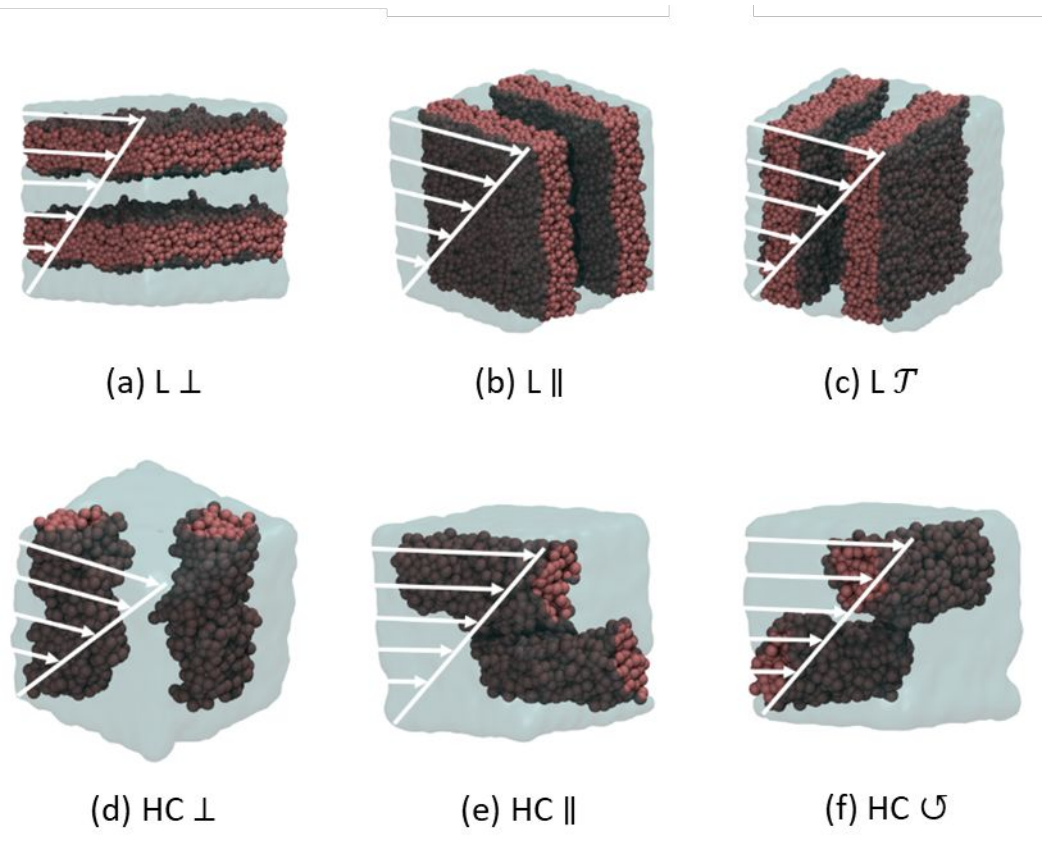

Figure 1. Illustration of the different shear orientations possible for Lamellae (L) morphology (a-c) and Hexagonal Cylinder (HC) (d-f). Beads from only the minority block are displayed for clarity.

In this paper, we study the effect of N and morphology on both the molecular diffusion and viscoelastic properties utilizing a coarse grained Molecular Dynamics (MD). The use of MD and model morphologies allow us to study the physical mechanisms underlying the different transport phenomena in the absence of major structural defects (i.e., within single-grain uniform structures). To form microphase separated structures with well-defined morphologies, χN should exceed the ODT value, which is efficiently achieved using a coarse-grained representation of the polymers. Using such a model, we were able to examine a wide range of segregation strengths and to probe the Rouse and reptation regimes. We find that, depending on temperature, the DBP properties transition from the Rouse regime to the reptation regime at a shorter N compared to isotropic melts, which we attribute to the topological constraint imposed by the interface between the two blocks that gives rise to an entanglement-like rheological signature (i.e., the onset of a plateau modulus). We also demonstrate the importance of block-

retraction to activate the lateral diffusion process for $N \gg N_e$ in L phase. Finally, in different DBP morphologies we show that trends in the anisotropic viscosity are correlated with the propensity for chain alignment with respect to the flow direction.

Methodology

Molecular Dynamic (MD) simulations were employed to study dynamic and viscoelastic properties of DBPs with various morphologies and chain lengths. All simulations were performed using LAMMPS.[35] The coarse-grained model adopted consists of beads and springs similar to that of Kremer and Grest for homopolymer melts but adapted to DBP systems. The bead-spring model has proven useful in studying viscoelastic, dynamic, and static properties of neat[12,13,36] and filled[6,37,38] polymer melts. Additionally, the model was successfully extended to study the phase behavior of DBP melts,[39,40,41] and the response of DBP networks to tensile deformation.[42,43,44]

To induce phase separation, like species interact via an attractive 6-12 Lennard-Jones potential, while unlike species interact via a purely repulsive potential known as the Weeks-Chandler-Andersen (WCA) potential.[39] Without loss of generality, the scaling quantities of mass (m), length (σ), and energy (ϵ) are set to unity, while the simulation quantities of concern are scaled as follows: temperature $T^* = k_b T/\epsilon$, time $t^* = t\sqrt{\epsilon/(m \cdot \sigma^2)}$, and number density $\rho^* = \rho\sigma^3$. The simulations were carried out in the canonical ensemble (NVT) with an integration time step (δt) of $0.001\,\tau$ using a Velocity-Verlet algorithm. T was controlled using the Nosé–Hoover thermostat, a suitable choice for studying transport properties due to its deterministic nature [45], with a damping parameter of $0.5\,\tau$. The three values used were $T = 2.63, 3.6$, and $5.0\ \epsilon/k_b$ which correspond to χ values of $3.5, 2.5$, and 1.8, respectively.[39] ρ was kept at $0.85\ \sigma^{-3}$, a value appropriate for polymer melts,[12,13,39] assuming incompressibility of the polymer across different N and T. Pressure isotropy was monitored to ensure that the box dimensions were appropriate to fit the natural domain periodicity of the system.[46]

The different DBP morphologies were realized by varying the volume fraction of the minority block ϕ_1 (Table 1). Details about system sizes and simulation box dimensions are provided in the

SI(*I*). A finite-size analysis of the self-diffusion coefficient is given in the SI(*II*) and confirms that finite-size effects would be negligible in our systems; self-diffusivity is used here as a representative probe as it is known to be a property quite sensitive to system size.[13]

Starting from a random configuration, the systems were allowed to equilibrate and achieve their equilibrium structure before any average property was calculated. The Gyroid (G) phase was an exception in that its initial configuration was obtained from a previous Dissipative Particle Dynamic (DPD) study by our group.[47] To confirm that we have the right equilibrated morphologies, the static structure factor ($S(\boldsymbol{q})$) was computed using eq. 1, where $\boldsymbol{q}$ is the wave vector (restricted to integer values of the wavelength), $\boldsymbol{r}_j$ is the position vector of bead j, and n is the total number of beads used in the calculation. The structure of all phases was visualized using VMD.[48]

$$S(\boldsymbol{q}) = \frac{\left(\sum_j \cos\left(\boldsymbol{q}\cdot\boldsymbol{r}_j\right)\right)^2 + \left(\sum_j \sin\left(\boldsymbol{q}\cdot\boldsymbol{r}_j\right)\right)^2}{n} \qquad (1)$$

Table 1. DBP simulated morphologies and their corresponding ϕ_1 and T_{ODT} (in units of ϵ/k_b)[39] for a given N.

N	ϕ_1 (T_{ODT})			
	Lamellae (L)	**Gyroid (G)**	**Hexagonal Cylinder (HC)**	**Sphere (S)**
10	0.5 (4.5)	–	–	–
14	0.5 (6.8)	–	–	–
18	–	0.33 (8.0)	–	–
24	0.5 (12.5)	–	0.25 (9.0)	–
32	0.5 (16.8)	–	–	–
40	0.5 (20.8)	–	0.25 (15.3)	0.10 (5.6)
50	0.5 (25.4)	–	–	–
60	–	–	0.25 (22.4)	–
64	0.5 (31.2)	–	–	–
76	0.5 (35.6)	–	0.25 (27.5)	–
Initial Configuration	Random	DPD structure	Random	Random

Equilibrium and non-equilibrium MD simulations were implemented to measure the properties of interest. The diffusion coefficient for motions parallel to the interface between the two blocks

($D_{\parallel}$) was computed in the L and HC phases. For the G phase and Homopolymer (HP), the isotropic diffusion coefficient (D_{iso}) was calculated. The diffusion coefficient (D) was found from the Mean Square Displacement ($\langle \Delta \boldsymbol{r}(t)^2 \rangle$) in equilibrium simulations using the Einstein relation of eq. 2, where $\langle \Delta \boldsymbol{r}(t)^2 \rangle$ is averaged over time origins (t_0), and b is the dimensionality of the space where motion is tracked (e.g., $b = 1$ for HC phase, 2 for L phase, and 3 for isotropic phases):[49]

$$D = \frac{1}{2b}\frac{d}{dt}\left\langle (\boldsymbol{r}(t + t_0) - \boldsymbol{r}(t_o))^2 \right\rangle_{t_0} \qquad (2)$$

D is computed when a linear relationship between $\langle \Delta \boldsymbol{r}(t)^2 \rangle$ and t develops, indicative of diffusive motion. The production period of the simulation ranged from $75{,}000$ to $100{,}000\tau$. For these calculations we only tracked the positions of the minority component bead connected to the majority component (i.e., the "interface bead"). Note that since we are only interested in the long-time diffusion, its value is largely independent on whether for the calculations we track the interfacial bead, the chain center-of-mass, or any other bead.

To compute η_0, G', and G'', non-equilibrium MD simulations were performed using the SLLOD equations of motion.[50] A combination of simple shear flow and oscillatory shear flow simulations were used to compute the zero-shear anisotropic viscosity components ($\eta_{0_{\alpha\beta}}$) using eqs. 3 and 4 below, where $\sigma^*_{\alpha\beta}$ is the stress tensor component in the flow direction α that is normal to velocity gradient direction β, $\dot{\gamma}_{\alpha\beta}$ is the strain rate, and ω is the oscillation frequency:

$$\eta_{0_{\alpha\beta}} = \lim_{\dot{\gamma}_{\alpha\beta} \to 0} \frac{\sigma^*_{\alpha\beta}}{\dot{\gamma}_{\alpha\beta}} \qquad (3)$$

$$\eta_{0_{\alpha\beta}} = \lim_{\omega \to 0} \sqrt{\left(G''_{\alpha\beta}\right)^2 + \left(G'_{\alpha\beta}\right)^2}/\omega \qquad (4)$$

The loss ($G''_{\alpha\beta}$) and storage ($G'_{\alpha\beta}$) moduli were calculated using eqs. 5-6, where $\sigma^*_{0_{\alpha\beta}}$ is the stress amplitude, $\gamma_{0_{\alpha\beta}}$ is the strain amplitude and δ is the phase lag. $\gamma_{0_{\alpha\beta}}$ in the oscillatory shear simulations was fixed to 10%, which ensures operating in the linear response regime where the Cox-Merz Rule applies[51] (see Figure S1 of *SI*(*III*)). $\sigma^*_{0_{\alpha\beta}}$ and δ were obtained from the least-square fit of the sinusoidal function (eq. 7) to the simulation data.

$$G''_{\alpha\beta} = \frac{\sigma^*_{0_{\alpha\beta}}}{\gamma_{0\alpha\beta}} \sin\delta \qquad (5)$$

$$G'_{\alpha\beta} = \frac{\sigma^*_{0_{\alpha\beta}}}{\gamma_{0\alpha\beta}} \cos\delta \qquad (6)$$

$$\sigma^*_{\alpha\beta} = \sigma^*_{0_{\alpha\beta}} \sin(t\omega + \delta) \qquad (7)$$

Results and Discussion

Figure 2 shows our results for D of DBPs with various morphologies and N values (listed in Table 1), including results for D of HP for comparison. Although only one result is available for the G phase, it clearly shows that its isotropic diffusion is significantly slower than that of the L phase, by a factor of ~ 2, a difference that is consistent with experimental findings and is attributable to the tortuosity of the G structure.[6,26] One unexpected observation in Figure 2 is that in the high-N regime chains diffuse faster in the HC phase than in the L phase. This may be due to the looser pinning of interfacial beads in the HC phase than in the L phase (as those beads in a curved interface partially experience the faster short-time dynamics of the nearby non-interfacial beads[52]), which facilitates the drift of long chains.

The trends in Figure 2 also indicate that DBPs with L morphology exhibits a transition from the Rouse regime to the reptation regime at a crossover chain length (N_c) that is shorter than that for HP. It is known that the onset of the reptation scaling occurs when $N_c \approx 2N_e$, where N_e is the entanglement chain length of HP. The slightly higher entanglement density of the L phase compared to the isotropic melt[25] cannot account for such "early" crossover (at $N_c \approx N_e$) suggesting that an alternative diffusion mechanism takes place in the L phase.

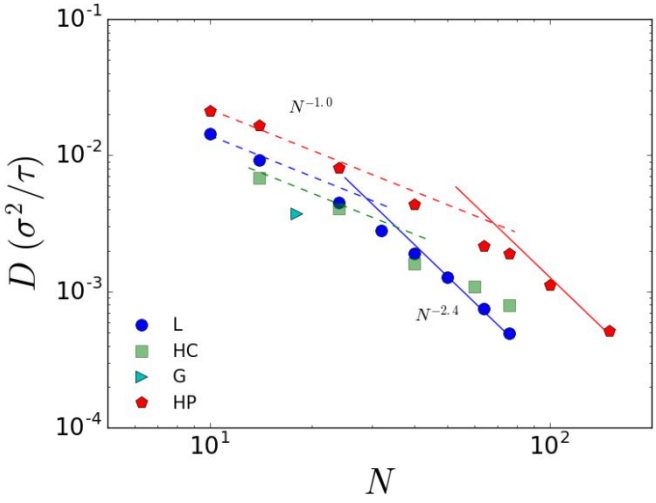

Figure 2. Effect of morphology and N on $D_{\parallel}$ for L and HC phases, and D_{iso} for G phase and HP at $T = 2.63\ \epsilon/k_b$. The dashed (solid) lines represent Rouse (reptation) scaling law. The error bars represent the standard deviation about the averages found for each system.

Dalvi et. al.[20] hypothesized that the lateral diffusion of an entangled L DBP melt proceeds via a block retraction mechanism, analogous to arm retraction in star polymers, where one block retracts to the interface in order for the chain to diffuse parallel to the interface plane. We tested this hypothesis by quantifying the effect on D of artificially reducing the tendency to block retraction. For this purpose, we pinned the end beads of either one block or both blocks to a stiff harmonic spring potential $\frac{1}{2}k(z_i - z_i^0)$ (with $k = 400\ \epsilon/\sigma^2$) to restrict chain motions only in the direction normal to the interface (Z). The preferential Z position (z_i^0) for each of the affected end beads was taken to be its initial value in an equilibrated structure. Figure 3a shows the probability distribution of the center-of-mass position of one block in the Z direction (COM_z) when the pinning springs are or are not enacted. For the pinned case, the probability distribution was averaged over chains with similar z_i^0 (within $\pm\ 0.5\ \sigma$), whereas all the chains were used for the unpinned "free" system. The COM_z variance for the constrained system is about half that for the free system. As shown in Figure 3b, for $N = 200$, the springs hinder the lateral motion significantly whether one block or both blocks are pinned. As expected from the behavior of trapped entangled systems, $\langle \Delta r^2 \rangle_{\parallel}$ approaches a plateau value of $a^2 N_e$ (i.e., the squared diameter of the tube). On the other hand, for $N = 10$ (i.e., a non-entangled system), ($\langle \Delta r^2 \rangle_{\parallel}$) is

not affected by the springs (Figure 3c). Overall, these results indicate that for entangled chains the cooperative motion of both blocks is required to activate the lateral diffusion process, further suggesting that the tubes formed by the entangled melt are preferentially aligned normal to the interface. Given that block retraction (taking place in the direction normal to the interface) is an essential component to the diffusion process of entangled self-segregated DBPs, we hypothesize that the pinning effect of the interface acts as a topological constraint akin to entanglements. In other words, the interface participates in the construction of the entanglement tube by preferentially aligning it in the direction normal to the interface. This would hence explain the "early" crossover from Rouse to reptation scaling seen in Figure 1 for the L morphology ($N_c \approx 1 N_e$) compared to HP ($N_c \approx 2N_e$).

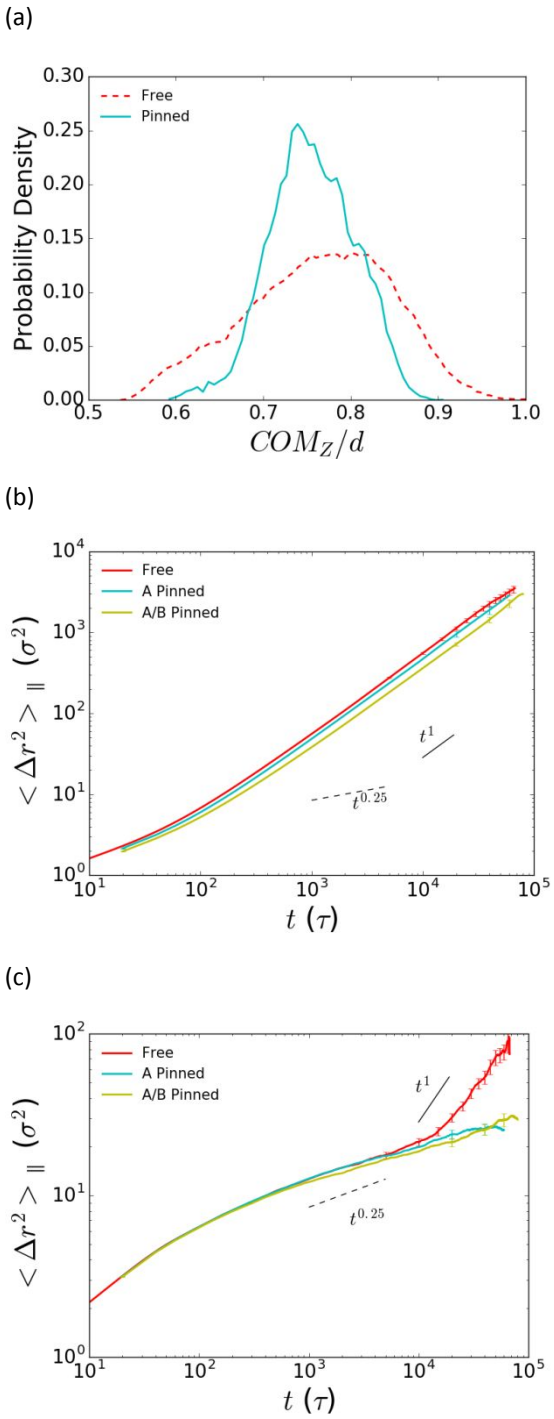

Figure 3. Effect of pinning potential on (a) the COM_z/d probability distribution of one block for $N = 200$, where the interface is located at $COM_Z/d = 1.0$, and on $\langle \Delta r^2 \rangle_{\parallel}$ for (b) $N = 200$ and (c) $N = 10$, where solid and dashed lines illustrate t^1 (diffusive motion) and $t^{0.25}$ (entangled motion) scaling, respectively. The error bars represent the 95% confidence interval of the averages found for the population of chains in the system.

To further test our hypothesis that the interface has the same effect on the dynamics of polymer melt as an entanglement, we examine the effect of DBP segregation strength on N_c by varying T. Note that T is related to segregation strength in DBPs but has no effect on N_c for HP as shown in Figure 4 (which includes the simulation data from Bulacu et al.[53]). As shown in Figure 5a, N_c increases with T and, based on the interface-effect, it is expected that at $T \gg T_{ODT}$, the behavior should approach that of HP. The effect of T on the segregation strength of the L phase can be captured by measuring the interfacial thickness (Δ), which is related to χN,[54] by fitting the order parameter $\psi(z)$ (eq. 8) to eq. 9, where $\phi_i(z)$ is the volume fraction of component i in the Z direction, and z_0 is the position at which $\phi_A(z) = \phi_B(z)$:[21]

$$\psi(z) = (\phi_A(z) - \phi_B(z))/(\phi_A(z) + \phi_B(z)) \qquad (8)$$

$$\psi(z) = \tanh\left(2(z - z_0)/\Delta\right) \qquad (9)$$

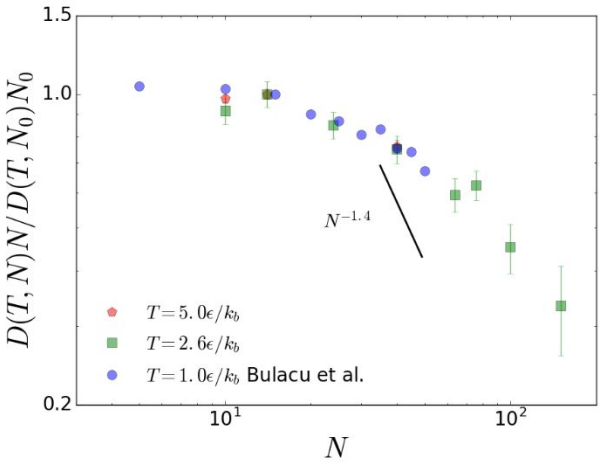

Figure 4. The effect of T on the dependence of $D \times N$ on N for HP. The effect of T is normalized for by a reference system ($N_0 = 14$) at the particular T. The solid line represents the reptation scaling ($N^{-1.4}$). The error bars represent the standard deviation about the averages found for the chain population in each system.

As shown in Figure 5b, Δ increases with T (for any N) until reaching a plateau value that is dependent on T. Since for the same T range, N_c is independent of T for HP, we attribute the change in N_c with T for DBPs to changes in the segregation strength as captured by the Δ trends in Figure 5b. The results from Figure 5a for $T = 2.63\ \epsilon/k_b$, where Δ is weakly dependent on N

(Figure 5b), indicate that $N_c \geq N_e$ since one constraint needs to come from a "true" entanglement for the crossover to take place, hence, the crossover at $N_c \approx 30$ (i.e. where the Rouse and reptation scaling laws intersect in Figure 2).

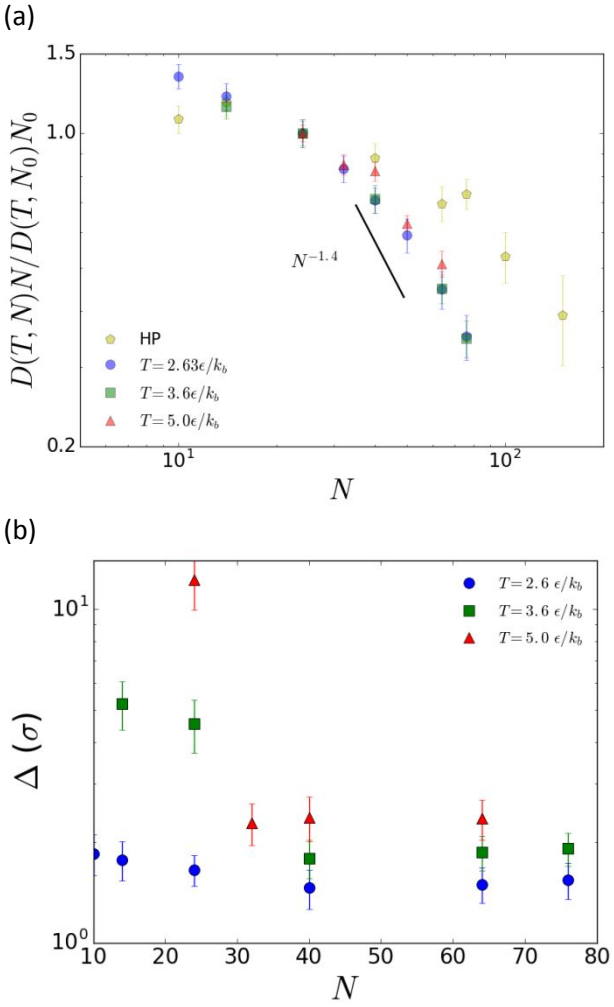

Figure 5. Effect of T on (a) the dependence of $D \times N$ with N for DBP having L morphology and HP, where the effect of T is normalized with respect to a reference system ($N_0 = 24$) at the particular T, and the solid line represents the reptation scaling ($N^{-1.4}$), and (b) the dependence of Δ with N for DBP having L morphology. Error bars represent the standard deviation about the averages from the different chains in the system in (a) and from the different configurations used in the calculation for (b).

Figure 6 shows the $G''_{\alpha\beta}$ and $G'_{\alpha\beta}$ moduli (eqs. 5 and 6) obtained from oscillatory shear simulations of the L phase. The first intersection of these curves (i.e., at small oscillation frequency (ω)) of G' and G'' is related to the entanglements' relaxation time (i.e.,

disentanglement), while the second intersection corresponds to the segment relaxation time between entanglements.[13,55] Figure 6(a-c) shows that for the L ∥ orientation no signs of entanglements are detectable for $N = 10 - 76$ where beads are expected to experience a nearly homogenous environment. However, in the L ⊥ and L $\mathcal{T}$ orientations (Figures 6(d-i)) for $N > 40$, an entanglement-like signature in the oscillatory shear modulus is observed, consistent with the topological constraint effect induced by the interface. To elucidate whether the modulus plateau of the L ⊥ and L $\mathcal{T}$ orientations is related to rubbery or cubic-phase behavior, dynamic oscillatory shear simulations of HP with $N = 200$ and 40 were conducted as a referential case pertinent to rubbery plateau behavior. The results shown in Figure 7 indicate, counter to trends observed in a previous experimental study of randomly oriented L grains,[34] that the modulus plateau of the HP is lower in magnitude than the modulus plateau found for the L ⊥ and L $\mathcal{T}$, and that the onset of the plateau takes place over a similar ω regime. Additionally, for L ∥ with $N = 200$ only one plateau is apparent, similar to the HP case. For HP with $N = 40$, no rubbery plateau is observed, suggesting that the apparent plateau in DBPs for $N < N_e$ is related to the presence of the interface. We note in passing that our oscillatory shear simulations for the G phase with $N = 18$ confirm the presence of a modulus plateau at terminal frequencies as found in experiments and attributed to the 3D lattice interconnectivity of the block domains.[34]

To confirm that the range of ω used is wide enough to capture the different relaxation time scales, we tested whether the calculated η_0 reached the Newtonian regime, which is a key tenet in our simulations. We show in the *SI*(*IV*) the mapping of our scaling quantities (m, ϵ, and σ) to a linear polyethylene melt by mapping N_c in our model to experimental data (Table S3). We then used these scaling quantities to predict D (Figure S2) and η_0 (Figure S3) and show that they agree with available experimental and atomistic simulations data for polyethylene.

The plateau modulus (G_N^0) can be related to N_e via the Rubber Elasticity theory:[55]

$$G_N^0 = \frac{4\rho k_b T}{5\ N_e} \approx G'(\min(\tan\delta)) \qquad (10)$$

resulting in $N_e \approx 11$ for the L ⊥ and L $\mathcal{T}$ orientations, independent of N above 40. At $T = 5.0\ \epsilon/k_b$, the oscillatory shear dynamics display no signs of entanglements for $N = 40$ (whose T_{ODT} is

$20.8\ \epsilon/k_b$ (Table 1)). These results again confirm that the interface in the strong segregation limit gives rise to an entanglement-like behavior that correlates with the crossover between the Rouse and reptation scaling regimes for D shown in Figure 2.

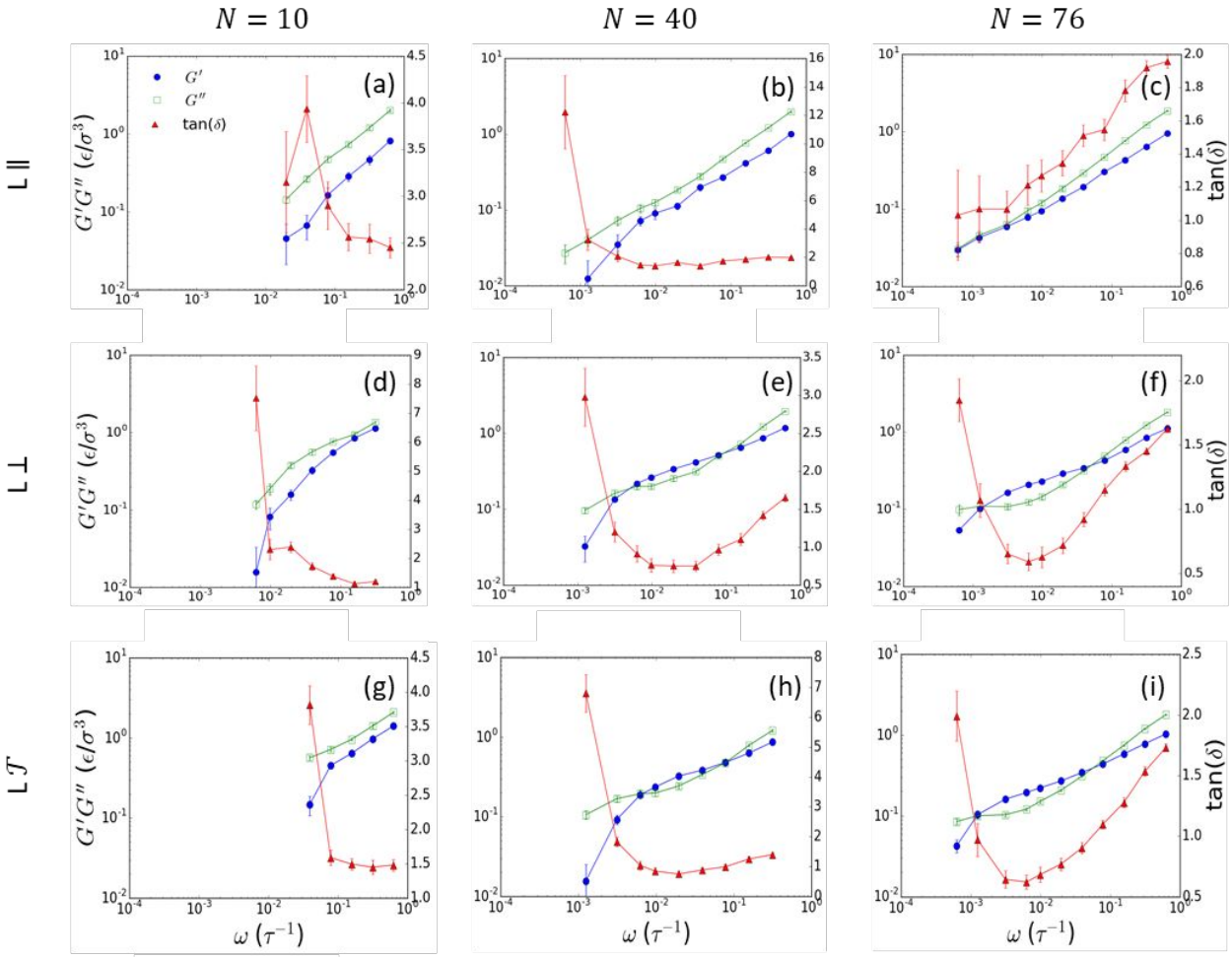

Figure 6. Effect of N and oscillatory direction on G',G'', and $\tan(\delta)$ for DBP with L morphology at $T = 2.63\ \epsilon/k_b$ and $\gamma_0 = 0.1$, where $\tan\delta = G''/G'$. For clarity, $\tan(\delta)$ is only shown for $N = 76$. Error bars for $L\perp$ and $L\mathcal{T}$ for $N = 40$ represent the 95% confidence interval for results from 12 uncorrelated initial configurations.

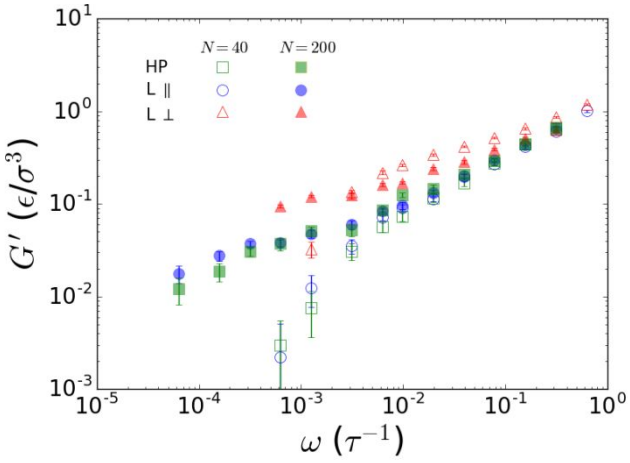

Figure 7. $G'_{\alpha\beta}$ of L ∥ and L ⊥ orientations compared to G' of HP case at $T = 2.63\ \epsilon/k_b$ and $\gamma_0 = 0.1$ for $N = 40$ and $N = 200$ obtained from dynamic oscillatory shear simualtions. Error bars represent the standard error from uncorrelated initial configurations. The results for the L$\mathcal{T}$ orienation, which are similar to those of the L ⊥ orientation, are not shown for clarity. See Figure 1 for nomenclature of shear orientations.

Another important property of polymeric materials that is strongly affected by entanglements is η_0. In Figure 8 we compare η_0 for HP obtained from steady shear simulations to the anisotropic zero-shear viscosity ($\eta_{0\alpha\beta}$) for DBPs with L and HC morphologies calculated via both steady and oscillatory shear simulations, and η_0 for Sphere (S) and G morphologies calculated via oscillatory shear simulations. It can be seen that no signs of reptation can be inferred from the scaling of the trends for all the morphologies and orientations, in agreement with the results from a previous study for homopolymer melts.[13] Figure 8 also shows that the viscosity of the HC ∥ and S phases are greater than that in the L ∥ phase, in agreement with a previous study.[32] η_0 for the S phase is smaller than that of HC ↺, possibly due to its reduced ϕ_1. For $N = 18$, G' of the G phase exhibits a plateau that spans several decades in frequency at low ω (consistent with experimental findings[34]), and as a result, η_0 diverges in the ω range examined. Since the flow direction in the L ∥, L ⊥ and HC ∥ orientations is not across the interface, we suspect that viscosity differences among them are connected to differences in how chains align relative to the flow direction. The larger viscosity values observed for the L$\mathcal{T}$, HC ↺, and S phases, where the flow direction is across

the interface, likely arises from energetic contributions to the stress response associated with unfavorable deformations of the interface structure.

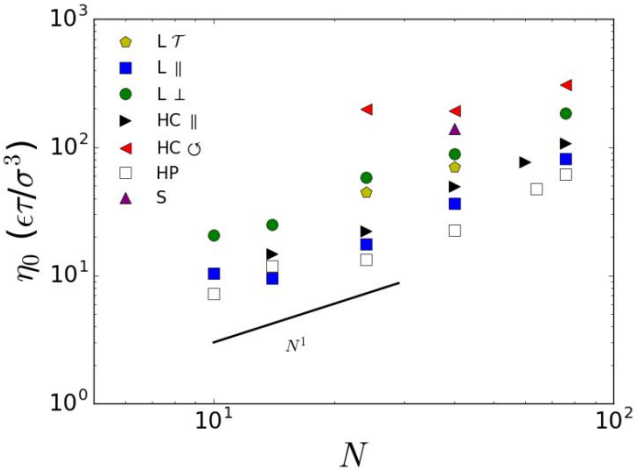

Figure 8. Zero-shear viscosity ($\eta_{0_{\alpha\beta}}$) for DBPs of different morphology and for homopolymer melt (HP), as a function of shear orientation and N at $T = 2.63\ \epsilon/k_b$. The straight line represents the Rouse scaling law (N^1).

In the HC phase, the majority block conformation is more isotropic, especially on the plane orthogonal to the cylinder axis, compared to the L phase where the blocks are distinctly more stretched in the direction normal to the interface than parallel to the interface. Figure 9 shows the distribution of the end-to-end distance (R_{ee}) in the three cartesian directions for the L (Figure 9a) and HC (Figure 9b) morphologies. No difference is observed between the parallel components of R_{ee} in the L phase and individual components of R_{ee} in the HC phase. We note that the use of cartesian coordinates, rather than cylindrical coordinates to analyze the components of R_{ee} in the HC phase, was intended to unveil correlations with the effect caused by a shear deformation being applied in directions aligned with the box' cartesian coordinates.

In the L ‖ orientation, the shear-flow neutral direction is normal to the interface. The viscosity in the L ‖ orientation is smaller than in the HC ‖ orientation because in the former chains are more aligned in the neutral direction and hence chain segments experience a smaller velocity gradient. Similarly, the L ⊥ viscosity is greater than those for the L ‖ and HC ‖ orientations because in the former chains are more aligned along the velocity gradient direction (i.e., the interface-normal direction). In Figure S6 of the *SI*(*V*), we further show that uniaxial deformation

simulations for the L and HC phases yield stress responses whose trends can be correlated to the same microscopic trends in chains conformations given here to explain the trends in viscosity from shear simulation results.

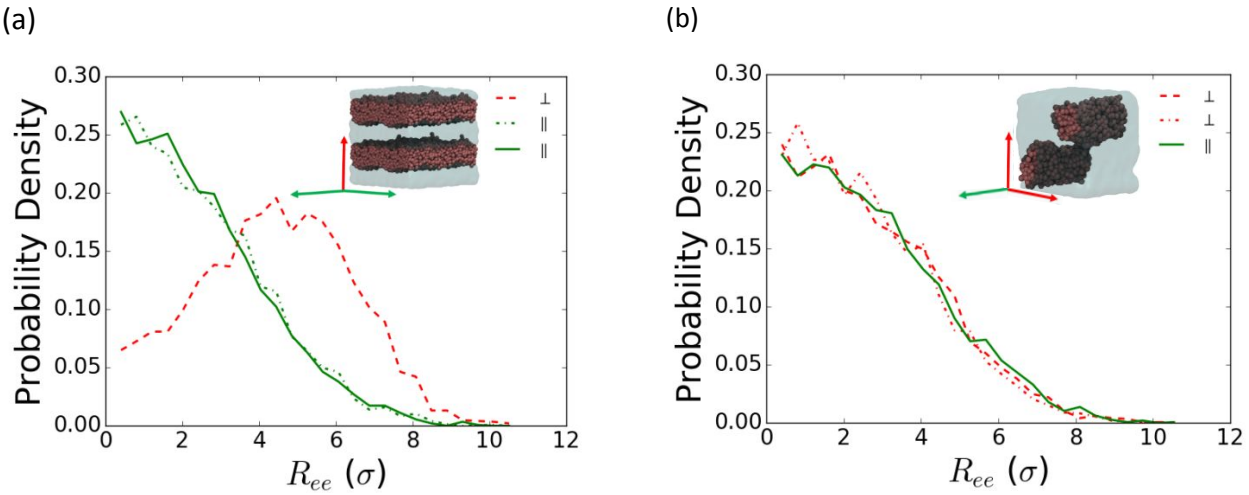

Figure 9. Distribution of the absolute value of the end-to-end distance of the majority block chains (R_{ee}) in the three cartesian directions for (a) L morphology and (b) HC morphology with $N = 40$ chains in the unperturbed state. The specific directions probed are depicted in the inset.

Conclusions

In this work, we examined first the role of DBP microphase separation on the onset of reptation scaling in D. We studied in particular detail the behavior of the diffusivity parallel to the interface in the L morphology. Specifically, we showed that in the strong segregation regime, the DBP interface constrains chain conformations in a way akin to topological constraints caused by entanglements, giving rise to a temperature-dependent early crossover from Rouse to reptation scaling (i.e. $N_c \approx N_e$ *vs.* $N_c \approx 2N_e$ in homopolymers). Our oscillatory shear simulations also showed an entanglement-like signature at the same N_c for the L $\perp$ and L $\mathcal{T}$ orientations. Given that a brush of mobile chains densely grafted to a flat surface, can be likened to a DBP lamellar layer, our results are loosely related to those of Lai et al.[56] who also showed that N_c for the lateral diffusion in a polymer brush depends on the grafting density with higher values resulting in earlier crossover.

We also found that the value of N_c for the diffusion coefficient increases with T as the segregation strength decreases in DBPs, in contrast to the $T-$ independent crossover behavior in HP. Our estimation of the interface thickness, which relates inversely with the segregation strength, confirmed that N_c is associated with N at which the interfacial thickness reaches a plateau at a given T. At low T, N_c becomes independent of T since at least two effective topological constraints are needed for the crossover to take place (i.e., one from the interface and at least one from the chain length).

In the entangled regime, we found that block retraction is an important mechanism in the diffusion of chains parallel to the L phase interface. In simulations designed to suppress fluctuations in chain extension normal to the interface, we found that the lateral mean square displacement of the interfacial bead approaches a plateau that is commensurate to the squared diameter of the tube in reptation theory, consistent with the tenet that block retraction is important to activate lateral diffusion. For chain lengths below N_e, the lateral diffusion was found to be independent of the block retraction motion. More generally, however, lateral diffusion of a given chain is likely a complex process that involves not only its retraction but also the cooperative motion of the surrounding neighbor chains. Further analysis of the effect of neighboring chains will be needed to identify in more detail the underlying mechanism of DBP diffusion in the entangled regime.

Analysis of steady and oscillatory shear simulations of different morphologies with different orientations revealed that the anisotropic zero-shear viscosity ($\eta_{0_{\alpha\beta}}$) mainly depends on chain alignment with respect to the "virtual" flow direction (by virtue of microphase separation) in the unperturbed state (i.e., zero shear), exhibiting a reduced value when chains are aligned in the flow or neutral direction. Moreover, the viscosity is always the largest when the shear flow direction is across the interface, likely due to additional energetic contributions associated with the stress response to interfacial deformations.

This work was concerned with describing the anisotropic stress response of DBPs to different modes of deformation (simple shear, oscillatory shear, and uniaxial elongation) and the direction of the deformation relative to orientation of the morphology. This study could be extended in a

number of different directions. For example, the uniaxial deformations simulated in this study (as reported in the *SI*(*V*)) have mainly probed the rubbery and solid-like response; however, performing a constant cross-section uniaxial elongation would be informative to probe adhesive properties.[57] It would also be interesting to perform simulations that probe the nano- and micro-rheology of DBP systems given the multiple length scales (such as d_T, Δ, and domain size) that define the structure of microphase separated morphologies. Such studies would allow to elucidate the interplay between the different length scales and the dynamics of nanoparticle probes with different size and moving at different speeds. Such insights would be relevant to understand the rheology of not only DBP melts but also DBP composites and electrolyte systems (whose macro-viscoelastic properties have little influence on the dynamics of the particles[37,57]). Work related to these topics is currently underway.

Acknowledgement

The authors acknowledge Prof. Claude Cohen and Mohammed Alhashim for insightful discussions. Mohammed Alshammasi acknowledges the Chemicals Admin Area of Saudi Aramco for sponsoring his education at Cornell University through the Advanced Degree Program. Support for computational resources and partial support of F. E. was provided by NSF DMREF Award Number 1629369.

References

1 N. Hadjichristidis, S. Pispas and G. Floudas, *Block Copolymers*, John Wiley & Sons, Inc., Hoboken, USA, 2002.
2 H. Feng, X. Lu, W. Wang, N.-G. Kang and J. Mays, *Polymers (Basel).*, 2017, **9**, 494.
3 M. D. Tikekar, S. Choudhury, Z. Tu and L. A. Archer, *Nat. Energy*, 2016, **1**, 16114.
4 E. D. Gomez, A. Panday, E. H. Feng, V. Chen, G. M. Stone, A. M. Minor, C. Kisielowski, K. H. Downing, O. Borodin, G. D. Smith and N. P. Balsara, *Nano Lett.*, 2009, **9**, 1212–1216.
5 W.-S. Young, W.-F. Kuan and T. H. Epps, *J. Polym. Sci. Part B Polym. Phys.*, 2014, **52**, 1–16.
6 M. S. Alshammasi and F. A. Escobedo, *Macromolecules*, 2018, acs.macromol.8b01488.
7 R. L. Weber, Y. Ye, A. L. Schmitt, S. M. Banik, Y. A. Elabd and M. K. Mahanthappa, *Macromolecules*, 2011, **44**, 5727–5735.
8 S. T. Milner, *Science (80-.).*, 1991, **251**, 905–914.
9 P. G. De Gennes, *J. Chem. Phys.*, 1971, **55**, 572–572.
10 P. G. De Gennes, *J. Chem. Phys.*, 1980, **72**, 4756–6387.
11 D. S. Pearson, G. Ver Strate, E. Von Meerwall and F. C. Schilling, *Macromolecules*, 1987, **20**, 1133–1141.
12 K. Kremer and G. S. Grest, *J. Chem. Phys.*, 1990, **92**, 5057–5086.
13 S. Sen, S. K. Kumar and P. Keblinski, *Macromolecules*, 2005, **38**, 650–653.
14 E. J. Amis and C. C. Han, *Polymer (Guildf).*, 1982, **23**, 1403–1406.
15 C. R. Bartels, B. Crist and W. W. Graessley, *Macromolecules*, 1984, **17**, 2702–2708.
16 C. B. Gell, W. W. Graessley, V. Efstratiadis, M. Pitsikalis and N. Hadjichristidis, *J. Polym. Sci. Part B Polym. Phys.*, 1997, **35**, 1943–1954.
17 J. Klein, *Macromolecules*, 1986, **19**, 105–118.
18 A. Ramírez-Hernández, F. A. Detcheverry, B. L. Peters, V. C. Chappa, K. S. Schweizer, M. Müller and J. J. de Pablo, *Macromolecules*, 2013, **46**, 6287–6299.
19 T. P. Lodge and M. C. Dalvi, *Phys. Rev. Lett.*, 1995, **75**, 657–660.
20 M. C. Dalvi, C. E. Eastman and T. P. Lodge, *Phys. Rev. Lett.*, 1993, **71**, 2591–2594.
21 M. Murat, G. S. Grest and K. Kremer, *Macromolecules*, 1999, **32**, 595–609.
22 M. Murat, G. S. Grest and K. Kremer, *Europhys. Lett.*, 1998, **42**, 401–406.
23 X. Pan and J. S. Shaffer, *Macromolecules*, 1996, **29**, 4453–4455.
24 V. Sethuraman, D. Kipp and V. Ganesan, *Macromolecules*, 2015, **48**, 6321–6328.
25 A. Ramírez-Hernández, B. L. Peters, L. Schneider, M. Andreev, J. D. Schieber, M. Müller, M. Kröger and J. J. de Pablo, *Macromolecules*, 2018, **51**, 2110–2124.
26 M. W. Hamersky, M. A. Hillmyer, M. Tirrell, F. S. Bates, T. P. Lodge and E. D. von Meerwall, *Macromolecules*, 1998, **31**, 5363–5370.
27 A. Nikoubashman, R. A. Register and A. Z. Panagiotopoulos, *Soft Matter*, 2013, **9**, 9960.
28 L. S. Shagolsem, T. Kreer and J.-U. Sommer, *ACS Macro Lett.*, 2014, **3**, 1201–1204.
29 L. S. Shagolsem, T. Kreer, A. Galuschko and J.-U. Sommer, *J. Chem. Phys.*, 2016, **145**, 164908.
30 A. Nikoubashman, R. L. Davis, B. T. Michal, P. M. Chaikin, R. A. Register and A. Z. Panagiotopoulos, *ACS Nano*, 2014, **8**, 8015–8026.
31 B. L. Peters, A. Ramírez-Hernández, D. Q. Pike, M. Müller and J. J. de Pablo, *Macromolecules*, 2012, **45**, 8109–8116.

32 K. Zhang and C. W. Manke, *Comput. Phys. Commun.*, 2000, **129**, 275–281.
33 J. H. Ryu, H. S. Wee and W. B. Lee, *Phys. Rev. E*, 2016, **94**, 032501.
34 M. B. Kossuth, D. C. Morse and F. S. Bates, *J. Rheol. (N. Y. N. Y).*, 1999, **43**, 167–196.
35 S. Plimpton, *J. Comput. Phys.*, 1995, **117**, 1–19.
36 M. Vladkov and J.-L. Barrat, *Macromol. Theory Simulations*, 2006, **15**, 252–262.
37 V. Kalra, F. Escobedo and Y. L. Joo, *J. Chem. Phys.*, 2010, **132**, 024901.
38 J. Liu, D. Cao and L. Zhang, *J. Phys. Chem. C*, 2008, **112**, 6653–6661.
39 M. A. Horsch, Z. Zhang, C. R. Iacovella and S. C. Glotzer, *J. Chem. Phys.*, 2004, **121**, 11455.
40 F. J. Martínez-Veracoechea and F. A. Escobedo, *J. Chem. Phys.*, 2006, **125**, 104907.
41 A. Chremos, A. Nikoubashman and A. Z. Panagiotopoulos, *J. Chem. Phys.*, 2014, **140**, 054909.
42 C. Nowak and F. A. Escobedo, *Phys. Rev. Mater.*, 2017, **1**, 035601.
43 C. Nowak and F. A. Escobedo, *Macromolecules*, 2016, **49**, 6711–6721.
44 B. M. Aguilera-Mercado, C. Cohen and F. A. Escobedo, *Macromolecules*, 2014, **47**, 840–850.
45 J. E. Basconi and M. R. Shirts, *J. Chem. Theory Comput.*, 2013, **9**, 2887–2899.
46 A. J. Schultz, C. K. Hall and J. Genzer, *J. Chem. Phys.*, 2002, **117**, 10329–10338.
47 P. Padmanabhan, F. J. Martinez-Veracoechea, J. C. Araque and F. A. Escobedo, *J. Chem. Phys.*, 2012, **136**, 234905.
48 W. Humphrey, A. Dalke and K. Schulten, *J. Mol. Graph.*, 1996, **14**, 33–38.
49 A. Einstein, *Ann. Phys.*, 1905, **322**, 549–560.
50 D. J. Evans and G. P. Morriss, *Phys. Rev. A*, 1984, **30**, 1528–1530.
51 W. P. Cox and E. H. Merz, *J. Polym. Sci.*, 1958, **28**, 619–622.
52 V. Sethuraman, V. Pryamitsyn and V. Ganesan, *J. Polym. Sci. Part B Polym. Phys.*, 2016, **54**, 859–864.
53 M. Bulacu and E. van der Giessen, *Phys. Rev. E*, 2007, **76**, 011807.
54 A. N. Semenov, *Macromolecules*, 1993, **26**, 6617–6621.
55 C. Liu, J. He, E. Van Ruymbeke, R. Keunings and C. Bailly, *Polymer (Guildf).*, 2006, **47**, 4461–4479.
56 P.-Y. Lai and K. Binder, *J. Chem. Phys.*, 1991, **95**, 4379–4423.
57 S. Goyal and F. A. Escobedo, *J. Chem. Phys.*, 2011, **135**, 184902.

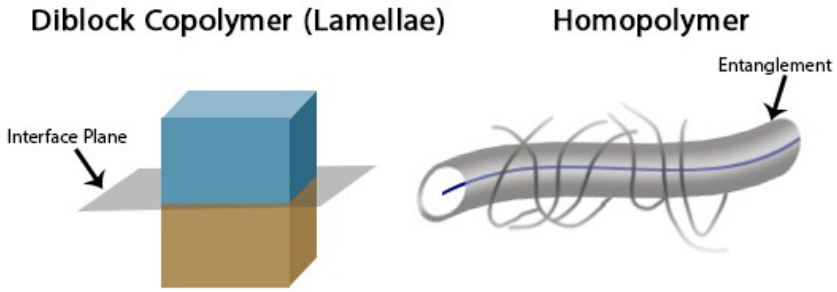

222x111mm (72 x 72 DPI)